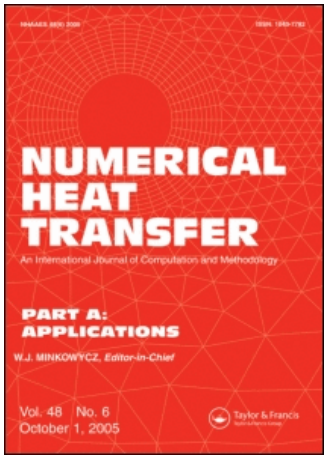

Numerical Heat Transfer, Part A: Applications
An International Journal of Computation and Methodology
Publication details, including instructions for authors and subscription information:
http://www.informaworld.com/smpp/title~content=t713657973

The Relationship Between the Distributions of Slot-Jet-Impingement Convective Heat Transfer and the Temperature in the Cooled Solid Cylinder

Neil Zuckerman [a]; Noam Lior [a]
[a] Department of Mechanical Engineering and Applied Science, University of Pennsylvania, Philadelphia, Pennsylvania, USA

Online Publication Date: 01 January 2008
To cite this Article: Zuckerman, Neil and Lior, Noam (2008) 'The Relationship Between the Distributions of Slot-Jet-Impingement Convective Heat Transfer and the Temperature in the Cooled Solid Cylinder', Numerical Heat Transfer, Part A: Applications, 53:12, 1271 - 1293
To link to this article: DOI: 10.1080/10407780801960373
URL: http://dx.doi.org/10.1080/10407780801960373

Numerical Heat Transfer, Part A, 53: 1271–1293, 2008

ISSN: 1040-7782 print/1521-0634 online
DOI: 10.1080/10407780801960373

THE RELATIONSHIP BETWEEN THE DISTRIBUTIONS OF SLOT-JET-IMPINGEMENT CONVECTIVE HEAT TRANSFER AND THE TEMPERATURE IN THE COOLED SOLID CYLINDER

Neil Zuckerman and Noam Lior
Department of Mechanical Engineering and Applied Science, University of Pennsylvania, Philadelphia, Pennsylvania, USA

A conjugate heat transfer investigation was conducted to better understand the effects of an impinging radial slot jet cooling device on both the heat transfer rates and temperature fields in the fluid, and especially in the cylindrical solid cooled by this device. The study used numerical methods to model a configuration in which a set of four radially positioned slot jets cooled a cylindrical steel target using air with a jet Reynolds number of 20,000. A steady-state v^2f Reynolds averaged Navier-Stokes model was used with a representative two-dimensional section of the axisymmetric target and flow domain. Boundary conditions, heat intensity, target wall thickness, and thermal conductivity were varied to study the effects of the impingement cooling on the temperature distribution in the solid. For Biot (Bi) numbers between 0.0025 and 0.073, temperatures in the solid were clearly affected by lateral conduction, and temperature variation in the solid was an order of magnitude smaller than the variation in the surface heat transfer coefficient. For the case of constant heat flux, the area-weighted standard deviation in the solid temperature was found to correlate well with the dimensionless parameter $Z \equiv Bi\left(d/t_{eq}\right)^2$, where d is the cylinder diameter and t_{eq} is the equivalent wall thickness, and a correlation equation was developed.

1. INTRODUCTION

The problem of heating or cooling solid bodies, including those having a curved surface, by impinging jets, is of interest in a variety of manufacturing processes and mechanical designs. Impinging jets are used for heat treatment, cooling and heating manufactured goods, temperature control of operating machinery, cooling of turbine blades and combustors, drying and defogging, and mass removal. Because of the resulting thinning of the boundary layer and the beneficial effect of the generated turbulence, impinging jets may achieve desired heat transfer rates with a flow an order of magnitude lower than conventional parallel-flow heat transfer designs. The physics and applications of these devices are detailed in many articles and a number of reviews [1–6]. At least as important as the rates of surface heat transfer and the associated convective heat transfer coefficients for single and

Received 4 April 2007; accepted 4 December 2007.
Address correspondence to Noam Lior, Department of Mechanical Engineering and Applied Science, University of Pennsylvania, 229 Towne Building, 220 S. 33rd Street, Philadelphia, PA 19104-6315, USA. E-mail: lior@seas.upenn.edu

NOMENCLATURE

B	slot jet nozzle width	t_{eq}	equivalent wall thickness
Bi	Biot number ($=ht/k$)	t_{scale}	turbulence time scale
$c_{\varepsilon 2}$	v^2f model constant	T	temperature
C_L	v^2f model constant	TR1, TR2, TR3	temperature ratio functions
C_η	v^2f model constant	U or u	fluid velocity component
C_μ	v^2f model constant	U_0	jet initial speed, average
C_1	v^2f model constant	v	fluid velocity
C_2	v^2f model constant	v^2 or $\overline{v^2}$	square of streamwise-normal velocity fluctuation
CFD	computational fluid dynamics	x	coordinate direction (x_i)
d	target diameter	y	distance from the wall
D	nozzle diameter	y^+	nondimensional distance from wall ($=y\tau^{0.5}\rho^{0.5}\nu^{-1}$)
D/Dt	material derivative		
f_{wall}	elliptic relaxation function	Z	correlation function $[\equiv \mathrm{Bi}(d/t_{eq})^2]$
h	convective heat transfer coefficient	α	v^2f model constant
H	nozzle-to-target spacing (nozzle height)	ε	turbulent kinetic energy dissipation rate
k	specific turbulent kinetic energy	θ_{az}	azimuth angle
k_c	fluid thermal conductivity	ν	fluid kinematic viscosity
L_{scale}	turbulence length scale	ν'	turbulent kinematic viscosity
$\mathrm{MAX}(\nabla T)^*$	nondimensional maximum temperature gradient magnitude	ρ	density
		σ	standard deviation function
		σ_ε	v^2f model constant
n	number of jets	τ	shear stress
$\hat{\boldsymbol{n}}$	wall-normal unit vector	**Subscripts**	
Nu	Nusselt number	amb	ambient
p	fluid pressure	avg	average (area-weighted)
p_s	static pressure	i	index number for cell or direction
p_t	total pressure	jet	properties at start of fluid jet
Pr	Prandtl number	min	minimum
Pr′	turbulent Prandtl number	max	maximum
q	dynamic pressure ($=\rho V^2/2$)	r	radial component (e.g., v_r)
q''	heat flux	t	turbulent (e.g., ν_t)
q'''	heat-generation rate, per unit volume	wall	value at target wall outer surface
r	radial position, measured from jet axis	θ	azimuthal component (e.g., v_θ)
Re	Reynolds number ($=U_0D/\nu$ for a jet)	0	at stagnation point
S_{ij}	strain rate tensor		
t	wall thickness		

multiple impinging jets, which have received much attention in the literature, are the resulting temperature and heat transfer distributions in the cooled or heated solid. This temperature distribution may result in phenomena of practical interest, such as nonuniform material properties, residual thermal stresses, and distortion of the target shape [4, 7]. Though numerical models of varying complexity have been developed and exercised to predict the fluid temperature in a variety of jet

impingement problems [8–13], the full conjugate heat transfer problem has been rarely modeled [14, 15]. As this aspect of impingement heat transfer has received little attention, its understanding is the main objective of this article.

The specific application of interest here is the cooling of a cylindrical target by surrounding it with an array of narrow slot jets aligned with the axis of the cylinder (Figure 1). This arrangement offers the potential to improve uniformity of heat transfer on the surface and provide high transfer rates on the entire cylinder surface. Though slot jet impingement has been studied frequently, relatively little has been published about this configuration with this particular nozzle and target combination. Our investigation was numerical. First, we conducted a literature search [5, 6] to understand the strengths and weaknesses of various numerical models applied to impinging jet problems. When using computational fluid dynamics (CFD), the presence, nature, and effects of turbulence are the most uncertain or difficult-to-model features of impinging jet flows. The available literature contains comparative studies of CFD turbulence models that were conducted with the goal of selecting the model best suited to the impinging-jet heat transfer configuration, though no single model has yet demonstrated all of the desired characteristics [16–19]. Common difficulties include overprediction of Nu in the stagnation region and underprediction of the intensity and size of the turbulent region in the wall jet shear layer, though models with realizability constraints (imposed limits on Reynolds stresses) have shown improved results [19].

Following the literature search, we performed CFD simulations of impinging jets. We used several existing time-averaged turbulence models, from the most common to several advanced ones, to examine their performance in simulating jet impingement cooling of a flat target under a round jet [20, 21], because experimental data were available for this configuration and could be used for numerical model error assessment (no suitable data were found for a cylindrical target). At the conclusion of this assessment, we selected the v^2f model as the best one from the

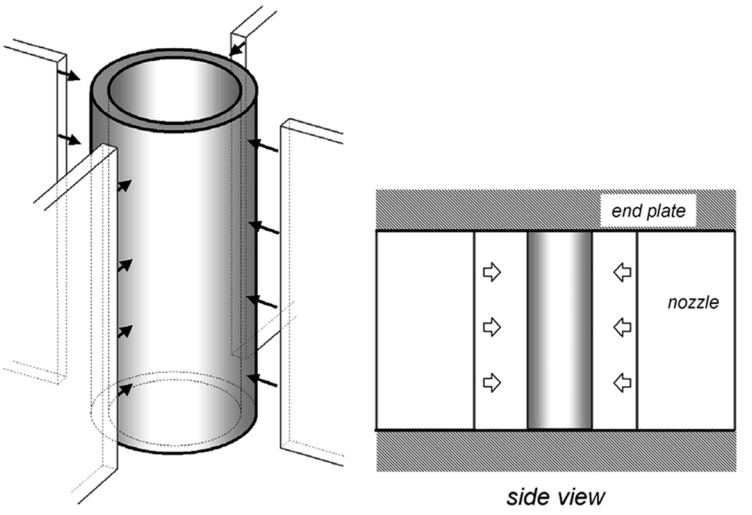

Figure 1. Isometric view and side view of target and slot jet nozzles.

standpoints of practicality and accuracy for further use (direct numerical simulation modeling would probably have produced better results but is impractical at this time for these Reynolds numbers), and constructed numerical models of a cylindrical target under various radial slot jet configurations. That study included the fluid domain only, and calculated the effects on Nusselt number of changes in nozzle size, target curvature, number of nozzles, jet speed, and Prandtl number [20, 21].

The model and other information from [20, 21], describing the convective heat transfer at the surface of a cylindrical target, were then used for the computation of the resulting temperature distribution within the solid target. Since there is little information about this temperature distribution, the focus of this article is the conjugate heat transfer study of the relationship between the target's impingement-induced convective surface heat transfer coefficients (or Nu) field and the target interior temperature distributions, as affected by heat conduction in the solid, and, in turn, of the effects of this conduction on the overall heat transfer and temperature distribution on the target surface. Specifically, we selected a jet configuration (Re, $H/2B$, $d/D, n$) and we varied the geometry and boundary conditions associated with the solid target. A significantly narrower scope version of this article was presented in [25].

2. MODEL CONFIGURATION

2.1. Governing Equations and Numerical Method

The computational model (governing equation set) for the fluid domain was based, after careful selection as explained above, on the v^2f turbulent fluid model available in Fluent 6.1.22 [22]. This model employs the common eddy-viscosity model equations for mass conservation and momentum conservation, along with equations for turbulent kinetic energy k, turbulence dissipation rate ε, streamwise-normal velocity variance v^2, and an elliptic relaxation function f which models the effects of walls upon v^2. The v^2f model is unique in that the turbulence-related increases in the diffusion of momentum and thermal energy are tied directly to v^2, rather than k (as is done with the k–ε model). The development of the important v^2 value is tied to the isotropic turbulent energy k, but also reduced by the presence of nearby walls via the term f.

As implemented, the model described the time-averaged behavior of an incompressible fluid with temperature-independent fluid properties. The governing equations of the v^2f model are presented in Eqs. (1)–(13).

$$\frac{\partial u_i}{\partial x_i} = 0 \tag{1}$$

$$\frac{Du_i}{Dt} = -\frac{\partial p}{\partial x_i} + \frac{\partial}{\partial x_j}\left[(\nu + \nu')\left(\frac{\partial u_i}{\partial x_j} + \frac{\partial u_j}{\partial x_i}\right)\right] \tag{2}$$

$$\frac{DT}{Dt} = \frac{\partial}{\partial x_i}\left[\left(\frac{\nu}{\mathrm{Pr}} + \frac{\nu'}{\mathrm{Pr}'}\right)\frac{\partial T}{\partial x_i}\right] \tag{3}$$

$$\frac{Dk}{Dt} = \frac{\partial}{\partial x_j}\left[(\nu + \nu')\frac{\partial k}{\partial x_j}\right] + 2\nu' S_{ij} S_{ij} - \varepsilon \tag{4}$$

$$\frac{D\varepsilon}{Dt} = \frac{c'_{\varepsilon 1} 2\nu' S_{ij} S_{ij} - c_{\varepsilon 2}\varepsilon}{t_{\text{scale}}} + \frac{\partial}{\partial x_j}\left[\left(\nu + \frac{\nu'}{\sigma_\varepsilon}\right)\frac{\partial \varepsilon}{\partial x_j}\right] \tag{5}$$

$$\frac{D\overline{v^2}}{Dt} = k f_{\text{wall}} - \overline{v^2}\frac{\varepsilon}{k} + \frac{\partial}{\partial x_j}\left[(\nu + \nu')\frac{\partial \overline{v^2}}{\partial x_j}\right] \tag{6}$$

$$f_{\text{wall}} - L^2_{\text{scale}}\frac{\partial}{\partial x_j}\frac{\partial f}{\partial x_j} = \frac{(C_1 - 1)\left(\frac{2}{3} - \frac{\overline{v^2}}{k}\right)}{t_{\text{scale}}} + \frac{C_2 2\nu' S_{ij} S_{ij}}{k} \tag{7}$$

$$S_{ij} = \frac{1}{2}\left(\frac{\partial u_i}{\partial x_j} + \frac{\partial u_j}{\partial x_i}\right) \tag{8}$$

$$\text{Pr}' = \left[0.5882 + 0.228\left(\frac{\nu'}{\nu}\right) - 0.0441\left(\frac{\nu'}{\nu}\right)^2\left(1 - e^{-5.165\nu/\nu'}\right)\right]^{-1} \tag{9}$$

$$\nu' = C_\mu \overline{v^2} t_{\text{scale}} \tag{10}$$

$$c'_{\varepsilon 1} = 1.44\left(1 + 0.045\sqrt{\frac{k}{\overline{v^2}}}\right) \tag{11}$$

$$L_{\text{scale}} = C_L \max\left[\min\left(\frac{k^{3/2}}{\varepsilon}, \frac{1}{\sqrt{3}}\frac{k^{3/2}}{\overline{v^2} C_\mu \sqrt{2 S_{ij} S_{ij}}}\right), C_\eta\left(\frac{\nu^3}{\varepsilon}\right)^{1/4}\right] \tag{12}$$

$$t_{\text{scale}} = \min\left[\max\left(\frac{k}{\varepsilon}, 6\sqrt{\frac{\nu}{\varepsilon}}\right), \frac{\alpha}{\sqrt{3}}\frac{k}{\overline{v^2} C_\mu \sqrt{2 S_{ij} S_{ij}}}\right] \tag{13}$$

where $C_\mu = 0.19$, $c_{\varepsilon 2} = 1.9$, $\sigma_\varepsilon = 1.3$, $C_1 = 1.4$, $C_2 = 0.3$, $C_\eta = 70.0$, $C_L = 0.3$, and $\alpha = 0.6$. In our case we solved for steady-state conditions, thus simplifying the material derivatives of Eqs. (2–6) to the form $u_i \partial()/\partial x_i$. Further details of the $v^2 f$ model are given in [23, 24] along with validation comparisons.

The authors had previously compared the $v^2 f$ model against the experimental data set of Baughn and Shimizu [26] to assess the $v^2 f$ model's accuracy [21]. It was found that the modeling error in the local heat transfer coefficient ranged from 2% in the wall jet to 26% in the stagnation region [20]. For the test case used, the total error in Nu_{avg} was 8%, averaged by area over the target surface. Additional studies were performed to examine the grid sensitivity of the results in the flat-plate

test case as well as a case with a ring of cylindrical jets, the configuration of interest described in Section 2.2 [21]. The grid sensitivity of the model was checked by increasing cell count and by changing shape functions, allowing either linear or quadratic variation of flow field properties across quadrilateral cells. Resulting profiles of Nu for the flat-plate model showed that doubling cell density or changing from first-order to second-order discretization changed local Nu values by no more than 4%, with changes in Nu_{avg} less than 1%. It was concluded that the model of the cylindrical configuration had measurable discretization error and that it affected the second significant figure of Nu_{avg}. Separate studies were performed to examine the influence of variable fluid properties on Nu_{avg}, by allowing variation in viscosity, density, and thermal conductivity of the fluid (air). For the cases of interest in the range of $1 < T_{wall}/T_{jet} \leq 4$, the resulting Nu_{avg} values changed by up to 3%, a second-order effect. These errors were considered acceptable, in view of the uncertainties in the available experimental data (such as the turbulence intensity in the approaching jet), and the typical errors in practical heat transfer correlations.

The two-dimensional steady conduction model assumed constant conductivity k_c and used the elliptic-type equation

$$k_c \frac{\partial}{\partial x_i} \frac{\partial T}{\partial x_i} + q''' = 0 \tag{14}$$

for the interior of the solid, where q''' represented a general heat source term in dimensions of power per unit volume (e.g., W/m^3).

Prior to use of the conjugate heat transfer model within Fluent, the conduction model was tested using a cylindrical target similar to the one to be used in the conjugate heat transfer study. The numerical solution was compared to that of closed-form analytical solution, and the modeling error of the conduction model was found to be less than 1%.

Steady Fluent solutions were performed using the segregated solver with implicit equations, standard pressure equations, the SIMPLE method for pressure–velocity coupling, and first-order-upwind differencing for the momentum, energy, and turbulent flow characteristics of each quadrilateral cell [22]. Underrelaxation was used for the pressure and momentum equations to provide stable convergence.

2.2. Geometric Configuration

A numerical model was developed to incorporate a cylindrical body of wall thickness t, which may represent a long annular cylinder of metal being continuously cooled, as shown in Figure 1. The section of the cylinder was modeled in two dimensions, and represented a central section of a cylindrical target located within an enclosure with end walls (Figure 2). The coolant flows within this enclosure. The mean flow velocities were constrained to a planar surface normal to the cylinder axis, and the mean velocity component in the axial direction was set as 0 (no axial flow because the cylinder was assumed to be very long). In addition to this assumption about symmetry in the axial direction, the geometric symmetry of the cross section was used to reduce the computational domain of the problem. The number of jets

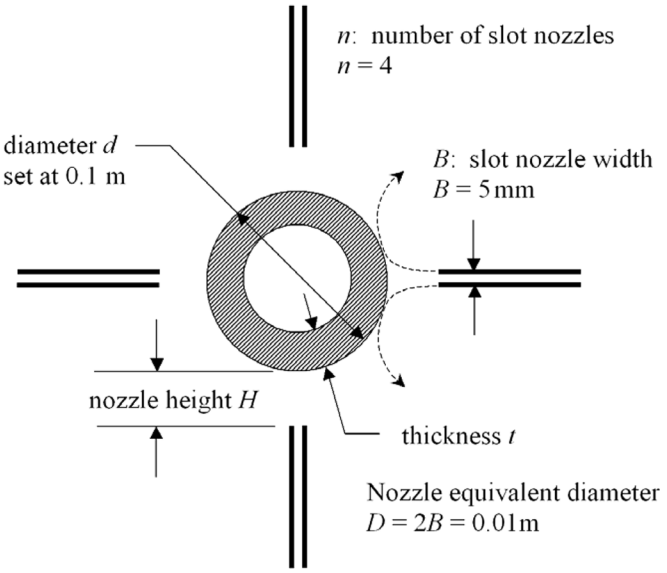

Figure 2. Model geometry for two-dimensional section of cylindrical target.

(n) was set at four, and it was assumed that all four jets had the same characteristics, and thus only one jet was modeled. The symmetry of the nozzle about its own center allowed further reduction of the domain, so that for the case with four nozzles, only 45° of circumference was included in the computational domain. The solution was then reflected about the center of the slot nozzle to cover 90° of circumference, and then rotated about the central axis by 90°, 180°, and 270° to fill the full 360° of azimuth.

The models were constructed using structured quadrilateral grids in two dimensions. The wall grid was constructed to yield y^+ values on the order of 1 in the first wall-adjacent cell, a requirement of the v^2f model for proper resolution of the boundary layer. Cell counts were in the range of 40,000 to 120,000 cells.

The cylinder outer diameter d was set to be 0.1 m. The ring outer radius r_o was 0.05 m and the wall thickness varied from 0.00125 m to 0.005 m. The nozzle length was set to be 0.05 m and nozzle width B was set to be 0.005 m (all are practical values for impingement cooling). The flow at the nozzle was set at 300 K and a uniform initial velocity with 1% turbulence intensity. This flow traveled through the nozzle, with the no-slip condition at the nozzle walls, until reaching the nozzle exit. The outflow region was modeled as a constant-static-pressure boundary, allowing backflow (due to possible entrainment) at a total pressure equal to the ambient static pressure.

2.3. Boundary Conditions and Material Properties

At the nozzle, the fluid temperature was assumed to be 300 K and the initial velocity uniform with 1% turbulence intensity. Fluid density and viscosity were

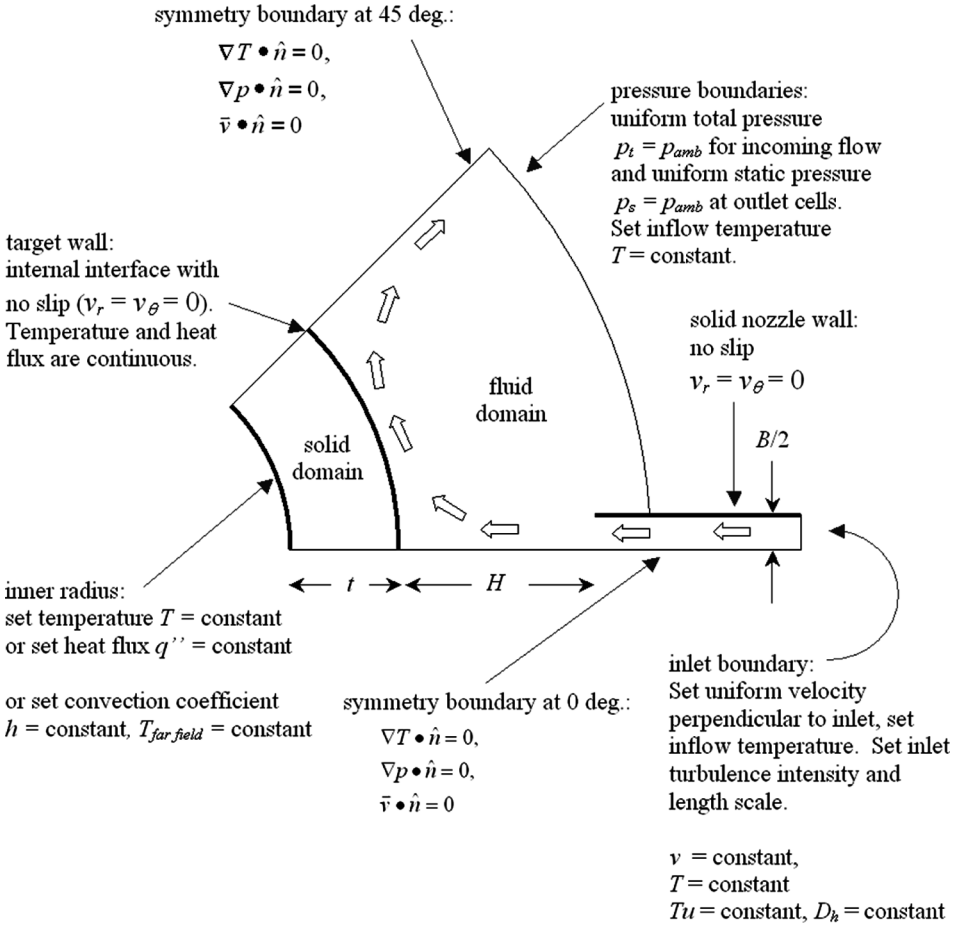

Figure 3. Computational domain for the conjugate heat transfer model.

set at constant values, which, as discussed in Section 2.1, causes an error of less than 3% in the range of parameters examined in this study. This flow through the nozzle was assigned a no-slip condition at the walls, until reaching the nozzle exit. The outflow region was modeled as a constant-static-pressure boundary, allowing backflow (due to possible entrainment) at 300 K with a total pressure equal to the ambient static pressure. The ambient pressure was set at 1 atm. As the results were correlated in a nondimensional form, the exact fluid properties were not critical to model validation.

The solid was represented as a material with uniform properties (uniform k_c) and no porosity or internal motion (velocity $v = 0$ within the solid). The energy equation used did not incorporate radiation effects; i.e., it was assumed that the temperature differences between the solid surface and the fluid were small, and the heat transfer coefficients relatively high, as they indeed were for these cases.

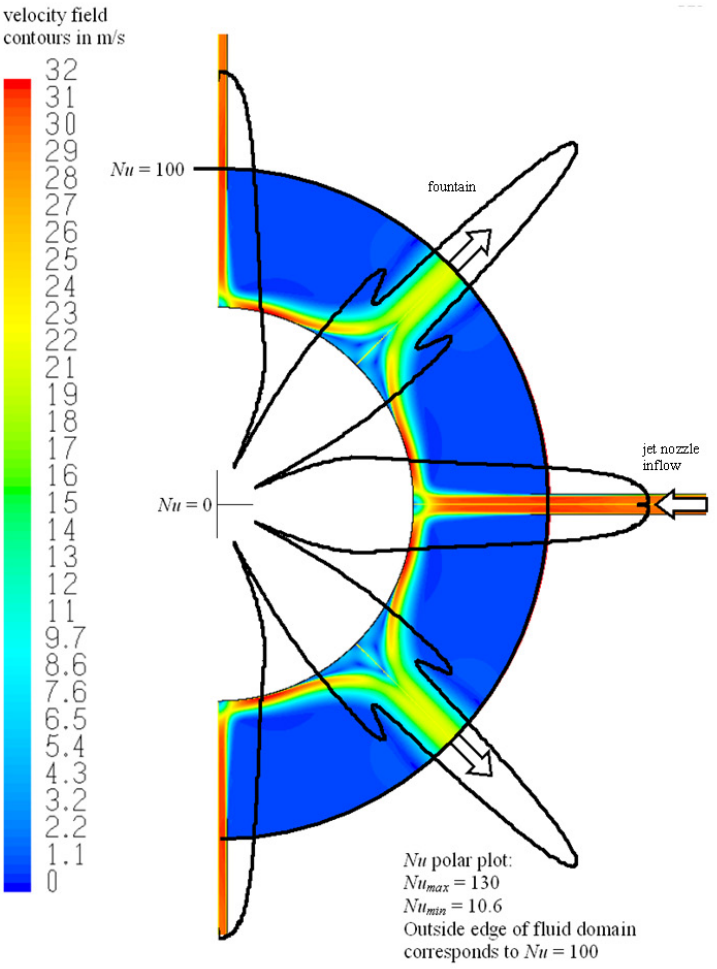

Figure 4. Fluid flow field—velocity distributions and Nu polar plot.

Figure 3 shows the computational region with all boundaries and boundary conditions.

At the target surface the velocity magnitude was made zero, and, consistent with conjugate solution methods, continuity of the temperature and heat flux at the interface between the adjacent solid and fluid cells was imposed.

Constant thermal conductivities and densities were selected for the solid and fluid. The conductivity of the steel target was first set at the software default value of conductivity, $k_c = 16.27\,\mathrm{W/m\,K}$. This value corresponded to a 26% nickel steel. To investigate the effect of the thermal conductivity of the solid, runs were also made for multiple steels with k_c from $10\,\mathrm{W/m\,K}$ (such as for a 40% nickel steel) up to $k_c = 73\,\mathrm{W/m\,K}$ (such as for a high-purity iron). The external flow field was set at $\mathrm{Re} = 20{,}000$, $n = 4$, $d/D = 10$. Parametric variations included type of heat source, solid material conductivity, material thickness, and heat source intensities.

To examine the constant properties assumption of the air, studies were performed using a fluid model with temperature-dependent viscosity, conductivity, and density (ideal gas equation). For the range of temperatures studied, these variations changed the temperature ratios and temperature standard deviations (described below) by several percent, indicating that fluid property variation affected only the second significant figure of the results.

Consistent with the steady-state assumption, three boundary conditions were assumed at the surface at the inner radius $r_i = (d/2) - t$ of the solid: (1) constant temperature $T(r_i)$ (here set at a uniform 700 K), (2) constant heat flux (here $q'' = 100\,\mathrm{kW/m^2}$), or (3) constant heat transfer coefficient h with uniform volumetric heat generation in the solid. Both the first and second boundary conditions are possible in laboratory tests but less common in actual practice, where one expects some intermediate condition, such as an inner wall surface with small variations in temperature and larger variations in local heat flux. The two extreme conditions selected thus served to bound the problem. The third boundary condition modeled that of a heat source uniformly distributed within the solid target with an intensity of $q''' = 10\,\mathrm{MW/m^3}$ ($10\,\mathrm{W/cm^3}$). This could represent a target with heating due to electrical current or nuclear reaction. The inner wall of the cylinder (r_i) was set in this case at a conservative transfer coefficient of $h = 12\,\mathrm{W/m^2\,K}$ to represent mild free convection to an environment at 300 K.

Calculations were performed to assess the model grid sensitivity of the conjugate model by running the model with 74,150 cells and then by halving cell length to produce 296,600 cells. The resulting exterior wall temperature changed by 0.5 K as a result. Based on the selection of first-order shape functions, it was estimated that further grid refinement beyond 74,150 cells would only change wall temperature by 1 K, a value which would only influence the second significant figure of the results. The convergence error was found to be at least an order of magnitude smaller than this discretization error. The required computation time varied from 1 to 10 h, using a 2-GHz Athlon 64 3200+ microprocessor running Windows XP Professional 2002 with 1 GB of RAM.

3. RESULTS

3.1 Fluid Flow and Temperature Fields

The resulting fluid flow field is shown in Figure 4 for half of the domain. The figure also includes an overlay of the Nusselt number profile as a polar plot. The stagnation region beneath the impinging jet had a high Nu. The wall jet adjacent to the stagnation region had progressively lower Nu in the flow direction until the flow separated from the surface. Following the separation, the jet formed a fountain before exiting in a radial direction. This fountain region had only a thin boundary layer and a high Nu in the recirculating region under the fountain.

As expected, the nonuniform cooling rate at the ring surface caused two-dimensional temperature nonuniformity within the wall of the annular cylinder. Figure 5 shows a typical contour map of temperature variations within sample targets with an imposed uniform heat flux of $q'' = 100\,\mathrm{kW/m^2}$ at $r_i = 0.045\,\mathrm{m}$ (note the relatively narrow temperature range plotted). At a given wall thickness, a change

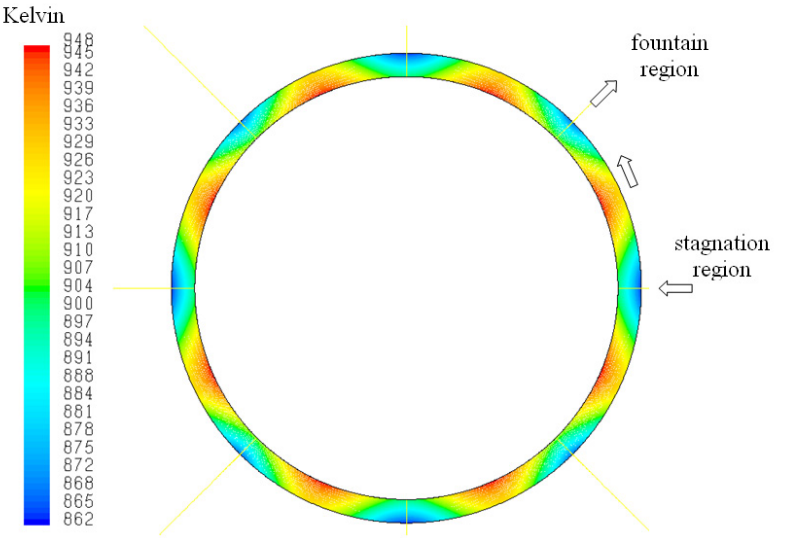

Figure 5. Typical temperature contours within the solid target in Kelvin for $t/d = 0.05$, $q''_{\text{inner}} = 100\,\text{kW/m}^2$, $k_c = 16.27\,\text{W/m K}$.

in conductivity changed the range of temperature within the target but otherwise had small influence on the pattern of the temperature contours. A change in thickness had a clear influence on the contour map, with a reduction in thickness causing the contours to be more pronounced in the radial direction, as circumferential conduction played a smaller role.

We compared our models with those of other impinging jet conjugate heat transfer studies, but due to significant differences in the geometry and physics, we found only a few similiarities. We briefly compared our steady-state results to that of the transient conjugate impinging-jet k–ω CFD study of Yang and Tsai [14]. In addition to the difference between the steady time-averaged and transient approaches, the two simulations differed in the basic target geometries, jet interaction effects, and turbulence models. Our simulations typically had 10 times the number of finite-volume cells used in [14]. The Reynolds numbers and solid wall heat fluxes were of the same order of magnitude, and so were the resulting heat transfer coefficients. Both simulations predicted the peak Nu in the stagnation region, but the jet interaction and curved surfaces of our cylindrical target resulted in boundary-layer separation and a fountain flow which brought about important differences in the Nu profile outside the stagnation region, as displayed in Figure 4. The later-time predictions of the transient model in [14] did not show the secondary peak in Nu found in steady-state experimental measurements [26]. During our original validation calculations we found this shortcoming to occur in the majority of RANS-type turbulence models, and we selected the v^2f model because of its ability to predict the secondary Nu peak, a feature that our models indicate occurs where the most turbulent region of the wall jet shear layer contacts the wall surface [21]. We also examined the conjugate heat transfer simulations of Rahman et al. [15], which modeled transient heat conduction due to the flow of a liquid free-surface

impinging jet at Re = 550 (laminar). This model showed low heat transfer rates in the center of the stagnation region, a characteristic associated with low turbulence and low fluid flow speed. In contrast, our high-Re submerged jet case involved a moderately turbulent stagnation region, as do most applications and simulations of gaseous impinging jets, in which turbulence is used to counteract the poor heat transport properties of stagnant and boundary-layer flows.

3.2. Temperature Variation and Uniformity

There are various ways to express temperature nonuniformity, and their definition and utility depend on the application. The temperature data were thus reduced to four different nondimensional criteria, labeled TR1, TR2, TR3, and σ, to describe the temperature nonuniformity in the solid, as shown in Eqs. (15)–(18):

$$\mathrm{TR1} = \frac{T_{\text{solid max}}}{T_{\text{solid min}}} \tag{15}$$

$$\mathrm{TR2} = \frac{T_{\text{solid max}} - T_{\text{solid min}}}{T_{\text{solid max}} - T_{\text{jet}}} \tag{16}$$

$$\mathrm{TR3} = \frac{T_{\text{solid max}} - T_{\text{solid min}}}{T_{\text{solid average}}} \tag{17}$$

$$\sigma = \sqrt{\frac{\sum_i A_i (T_i - T_{\text{average}})^2}{\left(\sum_i A_i\right)\left(T^2_{\text{average}}\right)}} \tag{18}$$

TR1 is the simplest of temperature ratios and incorporates no direct information about the external flow field. TR2 shows the ratio of temperature variation within the solid to that of the entire problem, yielding a number between 0 and 1. This creates a scale that incorporates the internal source effects and the cooling capability of the external flow. TR3 represents the temperature variation in proportion to the averaged temperature, showing a percent variation in temperature.

In addition to these minimum- or maximum-based functions, the spatial extent of temperature variations within the solid was characterized using a cross-sectional-area-weighted normalized standard deviation, σ, defined in Eq. (18), where A_i and T_i represent the individual cell area and cell-center temperature of each two-dimensional computational model cell. The summation was performed over all cells within the solid.

Further, the temperature gradient, which causes internal thermal stresses, was used as another nonuniformity criterion. Its distribution within the solid, and its maximum magnitude (where the highest thermal stresses may occur), were therefore computed and mapped for the cases studied. The maximum value of the gradient

magnitude was nondimensionalized as

$$\mathrm{MAX}(\nabla T)^* = \mathrm{MAX}\left(\sqrt{\frac{\partial T}{\partial x_j}\frac{\partial T}{\partial x_j}}\right)\frac{t}{(T_{\max} - T_{\mathrm{jet}})} \tag{19}$$

and calculated in each cell.

A typical temperature gradient magnitude contour map is shown in Figure 6. The highest T-gradient magnitudes were found in a thin layer of the solid directly under the jet and the fountain regions, where h was largest.

When making comparisons, the wall thickness was adjusted to match that of a common reference, a flat target with equivalent resistance using the equation $t_{\mathrm{eq}} = r_{\mathrm{inner}} \ln(r_{\mathrm{outer}}/r_{\mathrm{inner}})$, where r represents a wall radius of the solid. This allowed for comparison of the radial heat conduction through annular cylinders with slightly different inner wall radii. Various cylinders with equivalent d and equivalent t_{eq} would then have equivalent thermal resistance.

3.3. Influence of Parameters on Temperature Uniformity

The computations were made for the three boundary conditions described above. Table 1 lists the selected range of each variable parameter. A total of 37 models were used to cover these ranges. Numerical results are shown the Appendix, while the major effects of changing model parameters are summarized in Table 2. $\mathrm{Nu}_{\mathrm{avg}}$ was found to vary by no more than 3% among the various cases. For all boundary conditions, the maximum and average temperatures within the solid increased with an increase in source intensity [boundary conditions $T(r_i)$, q'', or q'''].

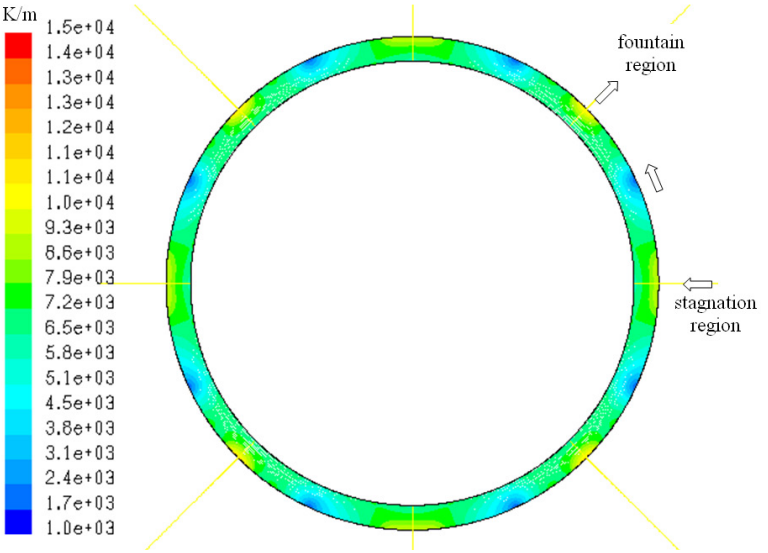

Figure 6. Temperature gradient magnitude contour map in K/m for $t/d = 0.05$, $q''_{\mathrm{inner}} = 100\,\mathrm{kW/m^2}$, $k_c = 16.27\,\mathrm{W/m\,K}$.

Table 1. Range of parameters varied during the study

Parameter	Symbol	Range of variation
Target thermal conductivity	k_c	10–73 W / m K
Ratio of wall thickness to target diameter	t/d	1.25–5 %
Local temperature in solid	T	307–1542 K
Boundary conditions, used one at a time:		
Inner boundary heat flux	q''	10–200 kW / m^2
Inner boundary temperature	$T(r_i)$	400–1500 K
Internal heat generation rate	q'''	0.25–40 MW/m^3
Observed ranges of results:		
Temperature ratio 1	TR1	1.001–1.35
Temperature ratio 2	TR2	0.007–0.357
Temperature ratio 3	TR3	0.001–0.298
Max gradient of T		0.009–0.177
Standard deviation of temperature	σ	0.0004–0.091
Surface heat transfer coefficient	h	151–159 W/m^2 K

The first ratio examined was TR1. For all three boundary conditions, the value of TR1 decreased with increasing k_c, as expected. For all boundary conditions, TR1 increased with an increase in source intensity. For the constant heat flux boundary condition, TR1 decreased with increasing equivalent wall thickness t_{eq}. For the constant heat-generation condition, TR1 decreased slightly with increasing t_{eq}. For the constant-temperature boundary condition, the effect was opposite: TR1 increased with increasing t_{eq}. The explanation for this behavior is that increasing t_{eq} while holding inner surface temperature constant reduced the outer wall surface temperature and hence reduced the influence of the magnitude of Nu. For the constant-temperature case, TR1 always decreased with decreasing Bi. For the constant heat-generation case, the increase in t_{eq} raised the total heat generated as the solid volume increased, and at the same time increased the thermal resistance. These two opposing effects caused only a minor change in TR1 with the increase of t_{eq}.

Table 2. Summary of the temperature ratio criteria sensitivity to parametric changes

Variable change	Boundary condition	TR1 response	TR2 response	TR3 response
k_c increase	Constant T	Decrease	Decrease	Decrease
k_c increase	Constant heat flux q''	Decrease	Decrease	Decrease
k_c increase	Constant heat generation q''	Decrease	Decrease	Decrease
t_{eq} increase	Constant T	Increase	Increase	Increase
t_{eq} increase	Constant heat flux q''	Decrease	Decrease	Decrease
t_{eq} increase	Constant heat generation q'''	Minor decrease	Decrease	No change
Heat source intensity increase	Constant T	Increase	No change	Increase
Heat source intensity increase	Constant heat flux q''	Increase	No change	Increase
Heat source intensity increase	Constant heat generation q'''	Increase	No change	Increase

For the constant heat flux boundary condition, an increase in t_{eq} caused an increase in the target thermal resistance and therefore elevated solid temperatures at the set flux.

Next the effects on TR2 and TR3 were examined. For all cases, the values of TR2 and TR3 decreased with increasing k_c (as expected and also seen for TR1). For all three boundary conditions, the value of TR3 increased with an increase in source intensity. The value of TR2, however, showed no significant change with source intensity for all three boundary conditions. This is understood from the fact that TR2 incorporated information about the full temperature scale of the problem from T_{max} to T_{jet} and thus became insensitive to the changes in T_{max} resulting from heat source intensity increases; TR2 was intended to scale with source intensity. For the case with constant heat flux, the values of both TR2 and TR3 decreased with increasing t_{eq}. This resulted primarily from the increase in the T_{max} or T_{avg} value caused by forcing the same flux through a higher resistance. For the case of constant heat generation, the value of TR2 decreased with increasing t_{eq}, but TR3 did not vary with t_{eq}. The effect on TR2 in this case resulted from scaling the model results with T_{max}, while the increase in thickness lowered the relative value of T_{min}. The minimal effect on TR3 was attributed to the competing influences of higher resistance and higher total power generation. For the constant-temperature boundary condition, the values of TR2 and TR3 both increased with increasing t_{eq}. This case was once again the opposite of the constant heat flux boundary condition, so increasing t at a given T_{max} produced a higher temperature drop through the target, allowing a lower T_{min} on the surface due to the increased relative influence of external convection (higher Bi). In comparison with TR2 and TR3, the majority of the values for TR1 had a small dynamic range. From this we concluded that TR3 provided a more useful and meaningful measure of the variation in surface temperature.

For all cases, an increase in k_c decreased the maximum gradient intensity, as expected. The method of nondimensionalizing the gradient magnitude made it invariant to source intensity. For all three boundary conditions, the magnitude of the maximal gradient increased with increasing t_{eq}. For the majority of cases, t_{eq} was within a few percent of t. Comparisons between models were performed using the Biot number defined as $\mathrm{Bi} = ht_{eq}/k_{c\,solid}$. Given the high conductivity of the metal target, the Bi for this application ranged from 0.0025 to 0.073. As a result, lateral conduction played an important role in smoothing out temperature variations in the solid. This effect is illustrated by the example profiles of T and Nu on the outer surface for the constant heat flux boundary condition, shown in Figure 7 for an example case with wall thickness $t/d = 0.05$. A comparable effect is seen in Figure 8 which shows inner and outer wall temperatures for the constant-temperature boundary condition at wall thicknesses $t/d = 0.05$ and $t/d = 0.025$. As the value of t increased and the outer surface temperature minima decreased, the regions of peak outer surface temperature also shifted farther away from the stagnation region.

Even though the local Nu varied by a factor of 10, the temperature variations in the solid were in the range of one-quarter to one-tenth of the overall temperature range in the problem. The regions of high fluid temperature (within 10% of the wall temperature) occupied only a small portion of the fluid volume within the computational domain boundary, shown in Figure 9, as the heat rapidly dropped off within

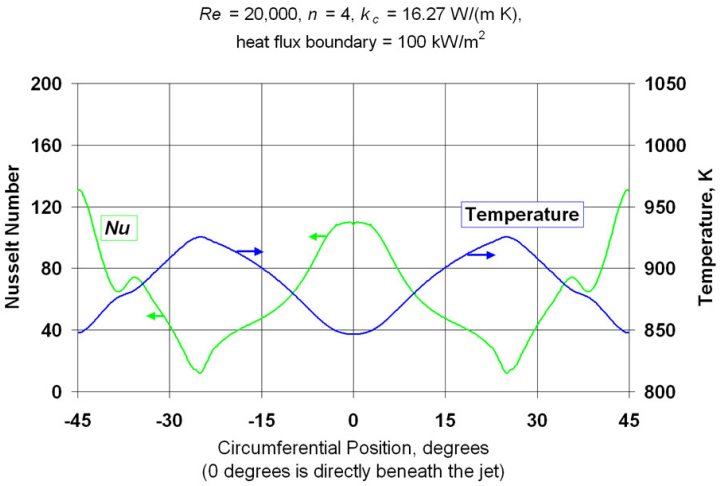

Figure 7. Nusselt number and temperature profiles on outer surface for $t/d = 0.05$, $q''_{\text{inner}} = 100\,\text{kW/m}^2$, $k_c = 16.27\,\text{W/m K}$.

the thermal boundary layer. The resulting Nu profile for the conjugate problem was very close to that found in the case of zero wall thickness [20, 21], with variations in Nu between cases in the studied range of only 1–3%. This showed that, within the range of variable values considered, conduction in the solid in the analysis has a negligible effect on the flow and heat transfer in the fluid, and on the convective heat

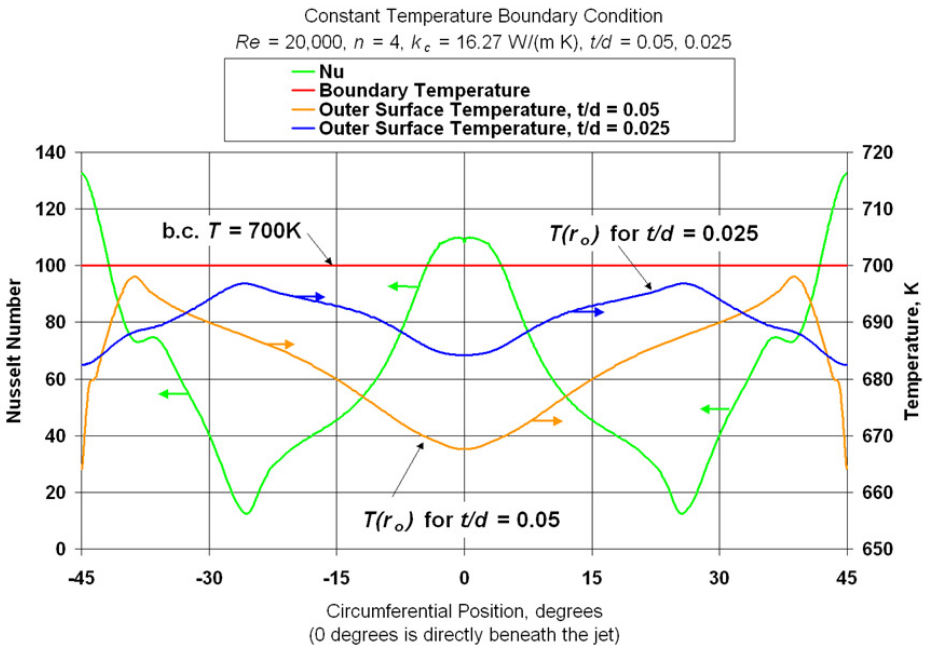

Figure 8. Nusselt number and temperature profiles on outer surface for $t/d = 0.05$ and 0.025, $T(r_i) = 700\,\text{K}$, $k_c = 16.27\,\text{W/m K}$.

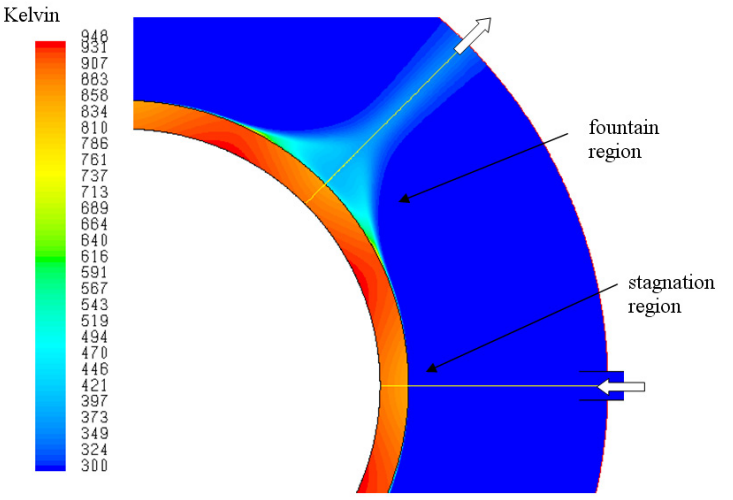

Figure 9. Contour map of temperature T in Kelvin for $t/d = 0.05$, $q''_{\text{inner}} = 100\,\text{kW/m}^2$, $k_c = 16.27\,\text{W/m K}$.

transfer coefficient on the solid interface. One practical conclusion is that it is not necessary to consider the conjugate problem if only the fluid dynamics and heat transfer in the fluid are of interest.

The Biot number Bi serves a useful purpose in describing the expected temperatures in the target. Further examination of the influence of k_c and t on the heat

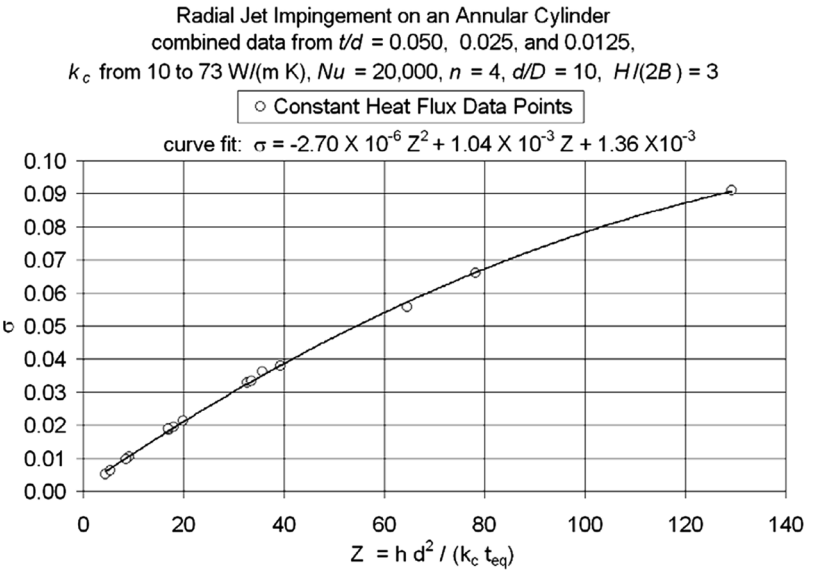

Figure 10. Standard deviation of temperature σ versus Z for $t/d = 0.050$, 0.025, and 0.0125, k_c from 10 to 73 W/m K.

distribution led to the conclusion that parameters describing uniformity of temperature did not and should not correlate with Bi, if we define Bi as $\mathrm{Bi} = ht_{eq}/k_c$. In general, the Biot number described the relative importance or strength of external convective transfer rate (h) to internal conductive heat transfer (k_c/t_{eq}). It did not incorporate any direct information regarding the uniformity within the target. To explain, as k_c is increased, and hence Bi decreased, it would be expected to obtain a more uniform temperature field within the solid target. Yet if t was increased, and Bi thus increased, it would also be expected to see a more uniform temperature within the target. So, a highly uniform temperature field could be associated with either high or low Bi, meaning Bi alone does not provide information allowing one to draw a conclusion about the expected temperature uniformity.

As stated above, the uniformity of the temperature was expected to increase both with increasing k_c and with increasing t_{eq}. Based on this relationship, a new nondimensional parameter was selected:

$$Z = \frac{h(d^2)}{kt_{\mathrm{eq}}} = \mathrm{Bi}\left(\frac{d}{t_{\mathrm{eq}}}\right)^2 \tag{20}$$

Because of the varying lateral conduction effects for the cylindrical geometry at different nondimensional thicknesses (t/d), the value of thickness t used in Eq. (20) was the equivalent flat-plate thickness t_{eq}.

Comparison of σ values versus Z for different k_c and t using the constant heat flux boundary condition showed a successful correlation, with all points falling on a single curve. One should note that the influence of variations in h and the nonuniformity of the h profile on σ were not investigated in this study. For this reason, the inclusion of h in the numerator was for convenience only; further studies should more thoroughly define the functional dependence on h (and thus k, t, n, Re, and t/d) and redefine the form of Z. Future work could then produce a new form of the Z function which would incorporate all of these independent variables, replacing h with another function, perhaps in a form incorporating both $h_{\max}$ and $h_{\min}$. The σ data for the other two boundary conditions did not correlate well with the form of Z shown in Eq. (20). It is likely that with more parameters incorporated into the Z function, it can be reformulated for problems with all three boundary conditions. Figure 10 shows the trend of σ versus Z for the constant heat flux boundary condition.

4 CONCLUSIONS

A conjugate heat transfer study of the effects of multiple (4) axial slot cooling jet impingement on a hot long cylindrical pipe was conducted. The study examined the temperature distributions and nonuniformities in the solid cylinder wall for $\mathrm{Re} = 20{,}000$, $10\,\mathrm{W/m\,K} \le k_c \le 73\,\mathrm{W/m\,K}$, $0.0125 \le t/d \le 0.0500$, $0.0025 \le \mathrm{Bi} \le 0.073$, and $4.4 \le \mathrm{Z} \le 129$. Despite the relatively large temperature difference of up to 400 K between the cooling fluid and the solid surface, the conduction in the solid was found to have a negligible effect on the flow and heat transfer in the fluid, and on the convective heat transfer coefficient on the solid interface. One practical

conclusion is that, for the range of parameters used in this study, it is not necessary to consider the conjugate problem if only the fluid dynamics and heat transfer in the fluid are of interest.

For the constant heat flux boundary condition on the internal pipe surface, the dimensionless parameter $Z \equiv \mathrm{Bi}(d/t_{\mathrm{eq}})^2$ was found to correlate well the internal temperature nonuniformity standard deviation σ with the values of k_c and t/d in that range. Defining and using several nonuniformity evaluation criteria, we found initial indications of the importance of lateral conduction in an annular cylinder cooled by radial impinging jets. For the cases studied herein, the lateral conduction played an important role in making the temperature nonuniformity in the solid an order of magnitude smaller than the nonuniformity in the surface Nu caused by the impinging jets.

REFERENCES

1. H. Martin, Heat and Mass Transfer between Impinging Gas Jets and Solid Surfaces, *Adv. Heat Transfer*, vol. 13, pp. 1–60, 1977.
2. K. Jambunathan, E. Lai, M. A. Moss, and B. L. Button, A Review of Heat Transfer Data for Single Circular Jet Impingement, *Int. J. Heat Fluid Flow*, vol. 13, pp. 106–115, 1992.
3. R. Viskanta, Heat Transfer to Impinging Isothermal Gas and Flame Jets, *Exp. Thermal Fluid Sci.*, vol. 6, pp. 111–134, 1993.
4. J. Ferrari, N. Lior, and J. Slycke, An Evaluation of Gas Quenching of Steel Rings by Multiple-Jet Impingement, *J. Mater. Process. Technol.*, vol. 136, pp. 190–201, 2003.
5. N. Zuckerman and N. Lior, Impingement Heat Transfer: Correlations and Numerical Modeling, *ASME J. Heat Transfer*, vol. 127, pp. 544–552, 2005.
6. N. Zuckerman and N. Lior, Jet Impingement Heat Transfer: Physics, Correlations, and Numerical Modeling, *Adv. Heat Transfer*, vol. 39, pp. 565–632, 2006.
7. H. Laschefski, T. Cziesla, G. Biswas, and N. K. Mitra, Numerical Investigation of Heat Transfer by Rows of Rectangular Impinging Jets, *Numer. Heat Transfer A*, vol. 30, pp. 87–101, 1996.
8. T. Cziesla, E. Tandogan, and N. K. Mitra, Large-Eddy Simulation of Heat Transfer from Impinging Slot Jets, *Numer. Heat Transfer A*, vol. 32, pp. 1–17, 1997.
9. A. Y. Tong, A Numerical Study on the Hydrodynamics and Heat Transfer of a Circular Liquid Jet Impinging onto a Substrate, *Numer. Heat Transfer A*, vol. 44, pp. 1–19, 2003.
10. N. Lior, The Cooling Process in Gas Quenching, *J. Mater. Process. Technol.*, vol. 155–156, pp. 1881–1888, 2004.
11. D. Sahoo and M. A. R. Sharif, Mixed-Convective Cooling of an Isothermal Hot Surface by Confined Slot Jet Impingement, *Numer. Heat Transfer A*, vol. 45, pp. 887–909, 2004.
12. I. Sezai and L. B. Y. Aldabbagh, Three-Dimensional Numerical Investigation of Flow and Heat Transfer Characteristics of Inline Jet Arrays, *Numer. Heat Transfer A*, vol. 45, pp. 271–288, 2004.
13. S. A. Salamah and D. A. Kaminski, Modeling of Turbulent Heat Transfer from an Array of Submerged Jets Impinging on a Solid Surface, *Numer. Heat Transfer A*, vol. 48, pp. 315–337, 2005.
14. Y.-T. Yang and S.-Y. Tsai, Numerical Study of Transient Conjugate Heat Transfer of a Turbulent Impinging Jet, *Int. J. Heat Mass Transfer*, vol. 50, pp. 799–807, 2007.
15. M. M. Rahman and A. J. Bula, Analysis of Transient Conjugate Heat Transfer to a Free Impinging Jet, *AIAA J. Thermophys. Heat Transfer*, vol. 14, pp. 330–339, 2000.

16. S. Polat, B. Huang, A. S. Mujumdar, and W. J. M. Douglas, Numerical Flow and Heat Transfer under Impinging Jets: A Review, *Annu. Rev. Fluid Mech. Heat Transfer*, vol. 2, pp. 157–197, 1989.
17. T. J. Craft, L. J. W. Graham, and B. E. Launder, Impinging Jet Studies for Turbulence Model Assessment—Part 2, An Examination of the Performance of Four Turbulence Models, *Int. J. Heat Mass Transfer*, vol. 36, pp. 2685–2697, 1993.
18. S. Z. Shuja, B. S. Yilbas, and M. O. Budair, Gas Jet Impingement on a Surface Having a Limited Constant Heat Flux Area: Various Turbulence Models, *Numer. Heat Transfer A*, vol. 36, pp. 171–200, 1999.
19. A. Abdon and B. Sundén, Numerical Investigation of Impingement Heat Transfer Using Linear and Nonlinear Two-Equation Turbulence Models, *Numer. Heat Transfer A*, vol. 40, pp 563–578, 2001.
20. N. Zuckerman and N. Lior, Jet Impingement Heat Transfer on a Circular Cylinder by Radial Slot Jets, Proc. IMECE05, 2005 ASME Int. Mechanical Engineering Congress and Exposition, Orlando, FL, November 5–11, 2005.
21. N. Zuckerman and N. Lior, Radial Slot Jet Impingement Flow and Heat Transfer on a Cylindrical Target, *AIAA J. Thermophysics Heat Transfer*, vol. 21, pp. 548–561, 2007.
22. Fluent, Inc., *Fluent 6.1 User's Guide*, 01-25-2003, 2003.
23. P. A. Durbin, A Reynolds Stress Model for Near-Wall Turbulence, *J. Fluid Mech.*, vol. 249, pp. 465–498, 1993.
24. P. Durbin, Separated Flow Computations with the k-ϵ-v^2 Model, *AIAA J.*, vol. 33, pp. 659–664, 1995.
25. N. Zuckerman and N. Lior, Heat Transfer and Temperature Distributions in the Fluid and Cooled Cylindrical Solid during Radial Slot Jet Impingement Cooling, Paper JET-05, 13th Int. Heat Transfer Conf., Sydney, Australia, August 13–18, 2006.
26. J. W. Baughn and S. Shimizu, Heat Transfer Measurements from a Surface with Uniform Heat Flux and an Impinging Jet, *ASME J. Heat Transfer*, vol. 111, pp. 1096–1098, 1989.

APPENDIX

Tables 3, 4, and 5 present quantitative results of the simulations with various parametric changes.

Table 3. Results from the conjugate heat transfer problem, constant heat flux boundary condition

Constant temperature		$n = 4, d = 0.1$ m, $Re_{jet} = 20,000$, $T_{jet} = 300$ K														
							TR1	TR2	TR3							
Boundary condition	k_c W/m K	t_{eq}/d	t/d	NU_{avg}	Z	Bi_{avg}	T_{max}/T_{min}	$(T_{max}-T_{min})/(T_{max}-T_{jet})$ Solid temperature range	$(T_{max}-T_{min})/(T_{avg\ solid})$ Solid temperature range	Max temp. gradient (non-dimensional)	σ	$n\sigma$ max	$n\sigma$ min	T_{max} in solid K	T_{avg} in solid K
$q'' = 100\,kW/m^2$	73	0.0474	0.0500	63	4.4	0.0098	1.02	0.033	0.022	0.029	0.0051	2.3	−2.1	909	898
$q'' = 100\,kW/m^2$	59	0.0474	0.0500	63	5.4	0.0122	1.03	0.041	0.028	0.035	0.0063	2.3	−2.1	912	898
$q'' = 100\,kW/m^2$	35	0.0474	0.0500	63	9.2	0.0206	1.05	0.066	0.046	0.058	0.0105	2.3	−2.1	921	899
$q'' = 100\,kW/m^2$	19	0.0474	0.0500	63	17.0	0.0382	1.09	0.115	0.082	0.100	0.0185	2.4	−2.1	941	901
$q'' = 100\,kW/m^2$	16	0.0474	0.0500	63	19.9	0.0447	1.10	0.132	0.095	0.114	0.0213	2.4	−2.1	948	902
$q'' = 100\,kW/m^2$	10	0.0474	0.0500	64	32.6	0.0733	1.16	0.197	0.148	0.170	0.0327	2.4	−2.1	977	905
$q'' = 100\,kW/m^2$	73	0.0244	0.0250	63	8.6	0.0051	1.03	0.047	0.033	0.013	0.0097	1.8	−1.6	944	927
$q'' = 100\,kW/m^2$	35	0.0244	0.0250	63	18.0	0.0107	1.07	0.093	0.066	0.026	0.0194	1.8	−1.6	959	927
$q'' = 100\,kW/m^2$	19	0.0244	0.0250	64	33.5	0.0199	1.12	0.157	0.115	0.046	0.0333	1.9	−1.6	983	925
$q'' = 100\,kW/m^2$	16	0.0244	0.0250	64	39.2	0.0233	1.14	0.177	0.132	0.053	0.0379	1.9	−1.6	991	925
$q'' = 100\,kW/m^2$	10	0.0244	0.0250	65	64.6	0.0384	1.22	0.253	0.198	0.080	0.0557	1.9	−1.6	1023	924
$q'' = 100\,kW/m^2$	73	0.0123	0.0125	63	16.9	0.0026	1.06	0.085	0.061	0.009	0.0189	1.6	−1.6	976	948
$q'' = 100\,kW/m^2$	35	0.0123	0.0125	64	35.6	0.0054	1.12	0.157	0.117	0.018	0.0362	1.6	−1.6	1001	946
$q'' = 100\,kW/m^2$	16	0.0123	0.0125	65	78.2	0.0119	1.24	0.271	0.214	0.034	0.0660	1.7	−1.6	1045	942
$q'' = 100\,kW/m^2$	10	0.0123	0.0125	66	129.2	0.0197	1.35	0.357	0.298	0.050	0.0910	1.7	−1.6	1086	940
$q'' = 10\,kW/m^2$	35	0.0474	0.0500	63	9.2	0.0206	1.01	0.065	0.011	0.058	0.0026	2.2	−2.0	362	360
$q'' = 200\,kW/m^2$	35	0.0474	0.0500	63	9.2	0.0206	1.06	0.066	0.055	0.058	0.0125	2.3	−2.1	1542	1499

Table 4. Results from the conjugate heat transfer problem, constant heat-generation condition

Constant temperature		$n = 4, d = 0.1$ m, $\mathrm{Re_{jet}} = 20,000$, $T_{jet} = 300$ K					TR1	TR2	TR3						
Boundary condition	k_c W/m K	t_{eq}/d	t/d	$\mathrm{NU_{avg}}$	Z	$\mathrm{Bi_{avg}}$	$\mathrm{T_{max}}/\mathrm{T_{min}}$	Solid temperature range $(\mathrm{T_{max}}-\mathrm{T_{min}})/(\mathrm{T_{max}}-\mathrm{T_{jet}})$	Solid temperature range $(\mathrm{T_{max}}-\mathrm{T_{min}})/(\mathrm{T_{avg\ solid}})$	Max temp. gradient (non-dimensional)	σ	$n\sigma$ max	$n\sigma$ min	$\mathrm{T_{max}}$ in solid K	$\mathrm{T_{avg}}$ in solid K
$q''' = 10\ \mathrm{MW/m^3}$	73	0.0474	0.0500	63	4.4	0.0098	1.01	0.027	0.014	0.029	0.0036	1.8	−2.0	598	594
$q''' = 10\ \mathrm{MW/m^3}$	59	0.0474	0.0500	63	5.4	0.0122	1.02	0.034	0.017	0.036	0.0044	1.8	−2.0	599	594
$q''' = 10\ \mathrm{MW/m^3}$	35	0.0474	0.0500	63	9.2	0.0206	1.03	0.055	0.028	0.058	0.0073	1.8	−2.0	602	594
$q''' = 10\ \mathrm{MW/m^3}$	19	0.0474	0.0500	63	17.0	0.0382	1.05	0.096	0.050	0.102	0.0128	1.8	−2.0	608	594
$q''' = 10\ \mathrm{MW/m^3}$	10	0.0474	0.0500	64	32.6	0.0733	1.09	0.164	0.088	0.177	0.0225	1.9	−2.0	620	595
$q''' = 10\ \mathrm{MW/m^3}$	73	0.0244	0.0250	63	8.6	0.0051	1.02	0.045	0.015	0.013	0.0048	1.6	−1.6	453	450
$q''' = 10\ \mathrm{MW/m^3}$	10	0.0244	0.0250	65	64.6	0.0383	1.09	0.236	0.089	0.080	0.0271	1.7	−1.6	469	448
$q''' = 0.25\ \mathrm{MW/m^3}$	35	0.0474	0.0500	63	9.2	0.0206	1.00	0.054	0.001	0.058	0.0004	1.8	−2.0	308	307
$q''' = 40\ \mathrm{MW/m^3}$	35	0.0474	0.0500	63	9.2	0.0206	1.05	0.055	0.045	0.058	0.0117	1.8	−2.0	1508	1477

Table 5. Results from the conjugate heat transfer problem, constant-temperature boundary condition

Constant temperature	$n = 4, d = 0.1\,\text{m}, \text{Re}_{\text{jet}} = 20,000, T_{\text{jet}} = 300\,\text{K}$														
							TR1	TR2	TR3						
Boundary condition	k_c W/m K	t_{eq}/d	t/d	NU_{avg}	Z	Bi_{avg}	$\text{T}_{\text{max}}/\text{T}_{\text{min}}$	Solid temperature range $(\text{T}_{\text{max}} - \text{T}_{\text{min}})/(\text{T}_{\text{max}} - \text{T}_{\text{jet}})$	Solid temperature range $(\text{T}_{\text{max}} - \text{T}_{\text{min}})/(\text{T}_{\text{avg solid}})$	Max temp. gradient (non-dimensional)	σ	$n\sigma$ max	$n\sigma$ min	T_{max} in solid K	T_{avg} in solid K
$\text{T}_{\text{inner wall}} = 700\,\text{K}$	73	0.0474	0.0500	62	4.4	0.0098	1.00	0.007	0.004	0.027	0.0022	4.7	2.8	700	693
$\text{T}_{\text{inner wall}} = 700\,\text{K}$	59	0.0474	0.0500	62	5.4	0.0121	1.00	0.007	0.004	0.034	0.0027	2.0	0.4	700	696
$\text{T}_{\text{inner wall}} = 700\,\text{K}$	35	0.0474	0.0500	63	9.1	0.0205	1.02	0.037	0.021	0.056	0.0045	2.0	−2.7	700	694
$\text{T}_{\text{inner wall}} = 700\,\text{K}$	19	0.0474	0.0500	63	16.9	0.0379	1.04	0.066	0.038	0.099	0.0082	2.0	−2.7	700	689
$\text{T}_{\text{inner wall}} = 700\,\text{K}$	16	0.0474	0.0500	63	19.7	0.0443	1.05	0.077	0.045	0.114	0.0095	2.0	−2.7	700	687
$\text{T}_{\text{inner wall}} = 700\,\text{K}$	10	0.0474	0.0500	63	32.2	0.0724	1.07	0.119	0.070	0.176	0.0150	2.0	−2.7	700	679
$\text{T}_{\text{inner wall}} = 700\,\text{K}$	73	0.0244	0.0250	63	8.5	0.0051	1.01	0.010	0.006	0.011	0.0012	2.0	−3.0	700	698
$\text{T}_{\text{inner wall}} = 700\,\text{K}$	16	0.0244	0.0250	63	38.3	0.0228	1.03	0.044	0.025	0.047	0.0052	1.9	−3.0	700	693
$\text{T}_{\text{inner wall}} = 700\,\text{K}$	10	0.0244	0.0250	63	62.6	0.0371	1.04	0.069	0.040	0.075	0.0082	1.9	−3.0	700	689
$\text{T}_{\text{inner wall}} = 400\,\text{K}$	35	0.0474	0.0500	63	9.1	0.0205	1.01	0.037	0.009	0.056	0.0020	2.0	−2.7	400	398
$\text{T}_{\text{inner wall}} = 1500\,\text{K}$	35	0.0474	0.0500	63	9.1	0.0205	1.03	0.037	0.030	0.056	0.0064	2.0	−2.7	1500	1481